Three-dimensional stacking of canted antiferromagnetism and pseudospin current in undoped math xmlns="http://www.w3.org/1998/Math/MathML">mrow>msub>mi>Sr/mi>mn>2/mn>/msub>msub>mi>IrO/mi>mn>4/mn>/msub>/mrow>/math>: Symmetry analysis and microscopic model realization

Yun-Peng Huang, Jin-Wei Dong, Ziqiang Wang, and Sen Zhou

Phys. Rev. B **104**, 165145 — Published 27 October 2021

DOI: 10.1103/PhysRevB.104.165145

Three-Dimensional Stacking of Canted Antiferromagnetism and Pseudospin Current in Undoped Sr_2IrO_4: Symmetry Analysis and Microscopic Model Realization

Yun-Peng Huang,[1, 2, *] Jin-Wei Dong,[1, 2, *] Ziqiang Wang,[3, †] and Sen Zhou[1, 2, 4, ‡]
[1] *CAS Key Laboratory of Theoretical Physics, Institute of Theoretical Physics, Chinese Academy of Sciences, Beijing 100190, China*
[2] *School of Physical Sciences, University of Chinese Academy of Sciences, Beijing 100049, China*
[3] *Department of Physics, Boston College, Chestnut Hill, MA 02467, USA*
[4] *CAS Center for Excellence in Topological Quantum Computation, University of Chinese Academy of Sciences, Beijing 100049, China*

Recent optical second-harmonic generation experiments observed unexpected broken spatial symmetries in the undoped spin-orbit Mott insulator Sr_2IrO_4, leading to intensive debates on the nature of its ground state. We propose that it is a canted antiferromagnetism with a hidden order of circulating staggered pseudospin current. Symmetry analysis shows that a proper c-axis stacking of the canted antiferromagnetism and the pseudospin current lead to a magnetoelectric coexistence state that breaks the two-fold rotation, inversion, and time-reversal symmetries, consistent with experimental observations. We construct a three-dimensional Hubbard model with spin-orbit coupling and structural distortion for the five localized $5d$ Wannier orbitals centered at Ir sites, and demonstrate the microscopic realization of the desired coexistence state in a wide range of band parameters via a combination of self-consistent Hartree-Fock and variational calculations.

I. INTRODUCTION

The layered square-lattice iridate Sr_2IrO_4 has been intensively studied since the discovery of the spin-orbit Mott state [1, 2], as a consequence of the interplay between spin-orbit coupling (SOC) and electron correlation[3–9]. The strong SOC of Ir atoms splits the t_{2g} orbitals into a fully-occupied $J_{\rm eff} = 3/2$ quartet and a half-filled $J_{\rm eff} = 1/2$ doublet. The latter is then localized by an otherwise moderate electronic correlation, realizing a single-band pseudospin-1/2 Heisenberg antiferromagnet (AFM) on the quasi-two-dimensional square lattice[1], with strong exchange couplings $J \sim 60$ meV[10]. This makes Sr_2IrO_4 a promising analog of the cuprates, and is thus expected to be another platform for unconventional superconductivity [11–14]. A remarkable range of cuprate phenomenology has been observed in both electron- and hole-doped Sr_2IrO_4, including Fermi surface pockets[15], Fermi arcs[16], pseudogaps[17, 18], and d-wave gaps[19, 20]. Whether a superconducting state exists as in the cuprates requires understanding thoroughly the correlated spin-orbit entangled electronic states observed in Sr_2IrO_4.

The ground state of the undoped Sr_2IrO_4 is of particular interest since it is the parent phase from which these novel spin-orbit entangled correlated states emerge. The electron correlation in the spin-orbit Mott state results in an insulating ground state with AFM long-range order. Neutron and resonant X-ray measurements reveal that the magnetic moments are aligned in the basal ab plane, with their directions tracking the $\theta \simeq 11°$ staggered IrO_6 octahedra rotation about the c axis due to strong SOC [21–25]. This gives rise to a net ferromagnetic (FM) moment along the a axis, in addition to the AFM component along the b axis. The magnetic structure in a IrO_2 layer is depicted schematically in Fig. 1(a). The net FM moment of each layer is shown to order in a $+--+$ pattern along the c axis[2, 26], where $\pm$ refers to the direction the FM moment along the a axis in each of the four IrO_2 planes in a unit cell. This magnetic ground state, hereinafter denoted as $+--+$ canted AFM (CAF), belongs to a centrosymmetric orthorhombic magnetic point group $2/m1'$ with spatial C_{2z} rotation, inversion, and time-reversal symmetries[27]. Recent optical second-harmonic generation (SHG) experiments [27], however, reported evidence of unexpected breaking of spatial rotation and inversion symmetries, pointing to the existence of a symmetry-breaking hidden order. It is argued that the broken symmetries can be caused by loop-currents [27–30] which were proposed to account for the pseudogap physics in the high-T_c cuprates [31–33]. However, the oxygen $2p$ states in Sr_2IrO_4 are much further away from (about 3 eV below) the Fermi level than those in the cuprates [1, 34], making it disadvantageous to develop the loop-currents that requires low-energy oxygen $2p$ states. Furthermore, the experimental measurements [27–30] suggest a magnetoelectric loop-current order that is ferrocially stacked along the c axis, which is incompatible with the recent observation [35] of a SHG signal that switches sign every two layers.

On the other hand, a different hidden order, the d-wave pseudospin current order (dPSCO), has been proposed to describe the band dispersion and the pseudogap phenomena observed in the electron-doped Sr_2IrO_4[36]. The dPSCO state generates circulating staggered pseudospin current with pseudospin-up electrons circulating in one direction and pseudospin-down electrons moving in the opposite direction, as illustrated in Fig. 1(b). This gives rise to a d-wave spin-orbit density wave and produces Fermi pockets and Fermi arcs in the nonmagnetic electron-doped Sr_2IrO_4, in good agreement with angle-resolved photoemission (ARPES) and scanning tunneling microscopy (STM) measurements [15–17, 19]. It was argued that the *d*PSCO is already present in the insulating magnetic phase of the undoped Sr_2IrO_4, responsible for the observed splitting of the bands [15] at $(\pi, 0)$ whose two-fold degeneracy is otherwise protected by certain lattice symmetries [36–38]. While describing remarkably well the highly unconventional quasiparticle properties observed in both the electron-doped and undoped Sr_2IrO_4, the *d*PSCO in Ref. [36] was considered in the two-dimension limit of a single IrO_2 plane. Further studies on the *c*-axis stacking of the *d*PSCO and the magnetic order in realistic three-dimensional systems are necessary in order to compare directly to the findings of the nonlinear optical experiments and the interpretation in terms of intracell loop-currents.

In this work, we discuss the symmetry properties of the *c*-axis stacking of CAF, *d*PSCO, and their coexistence, and study their microscopic realization in realistic three-dimensional models for undoped Sr_2IrO_4. The rest of the paper is organized as follows. In Sec. II, we perform symmetry analysis. We find that the particular coexistence state with $+--+$ CAF and $\oplus\oplus\ominus\ominus$ *d*PSCO has the symmetries consistent with experimental observations [27–29] in undoped Sr_2IrO_4. It is a magnetoelectric state that breaks the spatial two-fold rotation, inversion, and time-reversal symmetries. Considering all five $5d$ orbitals of the Ir atoms, a realistic three-dimensional tight-binding model including SOC (TB+SOC) is constructed in Sec. IIIA, which describes faithfully the low-energy band structure of Sr_2IrO_4 with the structural distortion. The Hubbard interactions are introduced in Sec. IIIB and treated within the Hartree-Fock approximation to account for the effects of electron correlations that generate magnetism spontaneously. We obtain CAF phases with different *c*-axis stacking pattern self-consistently and compare their energies. The $+--+$ CAF revealed in experiments is found to be energetically favored in a wide range of band parameters. In Sec. IIIC, the hidden *d*PSCO is considered phenomenologically by including a variational term in the Hamiltonian. We fix the stacking pattern of CAF to be $+--+$, and compare the energies of coexistence states with different *c*-axis stacking of *d*PSCO. The mostly favorable stacking pattern for *d*PSCO is found to be indeed the desirable $\oplus\oplus\ominus\ominus$, supporting the above-mentioned coexistence state as the ground state of undoped Sr_2IrO_4, with its symmetries consistent with experimental measurements. Discussions and summaries are presented in Sec. IV.

II. SYMMETRY ANALYSES

To be more precise, we denote the magnetic ground state of undoped Sr_2IrO_4 as $(+--+)_a$ CAF, where the subscript a specifies the direction of the net FM moment, since, in principle, it can be along either a or b axis[23, 24, 39]. Fixing the net FM moment along $\alpha = \{a, b\}$ axis, there are four possible relative stacking along the c axis of the FM in-plane component of the moment in each of the four IrO_2 planes in a unit cell, *i.e.*, $(+--+)_\alpha$, $(++--)_\alpha$, $(+-+-)_\alpha$, and $(++++)_\alpha$. It is easy to show that there is a one-to-one correspondence between states with FM moment along a axis and those with FM along b axis, by performing a C_{4z} rotation around the c axis and a lattice translation. Explicitly, the $(+--+)_a$, $(++--)_a$, $(+-+-)_a$, and $(++++)_a$ CAF state are equivalent to, respectively, $(++--)_b$, $(+--+)_b$, $(+-+-)_b$, and $(++++)_b$ CAF state. The correspondence shall be verified numerically later in the microscopic model calculations presented in Sec. IIIB by comparing the state energies. Therefore, without loss generality, we restrict the direction of the FM moments to be along a axis and drop the subscript for the CAF states in the rest of the paper, unless otherwise noted.

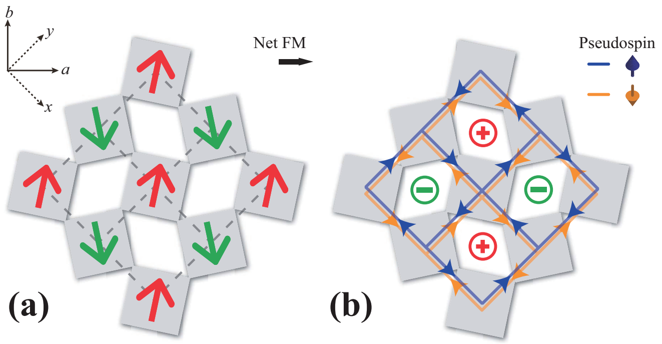

FIG. 1: Schematic topview of (a) the CAF and (b) the *d*PSCO state in a single IrO_2 plane. Shaded squares represent IrO_6 octahedra, whose staggered rotation about the c axis results in, structurally, two kinds of Ir sites and two kinds of Ir plaquettes. The red and green arrows in (a) denote the magnetic moments on these two kinds of Ir sites. The canting of the AFM moments leads to a net FM moment along the $+a$ axis, and, consequently, the magnetic structure shown in (a) is defined as "+" in the layered stacking pattern of the 3D CAF order. The blue and orange lines with arrows in (b) indicate the moving directions of the pseudospin-up and pseudospin-down electrons, respectively. The opposite motion of the electrons with opposite pseudospins creates circulating pseudospin current and staggered pseudospin flux through each Ir plaquette. The direction of the pseudospin flux through these two kinds of Ir plaquettes is denoted by, respectively, red and green symbols at the plaquette center, with $\oplus/\ominus$ corresponding to $\pm c$ axis. The direction of the pseudospin flux in the plaquette enclosing the red parallelogram is $\oplus$ in the dPSCO shown in (b), which is then defined as "$\oplus$" in the layered stacking pattern.

The symmetries of the CAF phases (without *d*PSCO) with different *c*-axis stacking are summarized in Table I(a), which gives the lattice translation, if exist, required

(a) Symmetries of *c*-axis stacked CAF:

stacking	C_{2z}	M_z	I	T	C'_{2z}	M'_z	I'
$+--+$	$\boldsymbol{\tau}_{xyz}$	$\boldsymbol{\tau}_{yz}$	0	$\boldsymbol{\tau}_{xyz}$	0	$\boldsymbol{\tau}_{x}$	$\boldsymbol{\tau}_{xyz}$
$++--$	$\boldsymbol{\tau}_{xyz}$	$\boldsymbol{\tau}_{x}$	$\boldsymbol{\tau}_{xyz}$	$\boldsymbol{\tau}_{xyz}$	0	$\boldsymbol{\tau}_{yz}$	0
$++++$	×	×	0,$\boldsymbol{\tau}_{xyz}$	×	0,$\boldsymbol{\tau}_{xyz}$	$\boldsymbol{\tau}_{x}$,$\boldsymbol{\tau}_{yz}$	×
$+-+-$	×	$\boldsymbol{\tau}_{x}$,$\boldsymbol{\tau}_{yz}$	×	×	0,$\boldsymbol{\tau}_{xyz}$	×	0,$\boldsymbol{\tau}_{xyz}$

(b) Symmetries of *c*-axis stacked *d*PSCO:

stacking	C_{2z}	M_z	I	T	C'_{2z}	M'_z	I'
$\oplus\ominus\ominus\oplus$	0	$\boldsymbol{\tau}_{x}$	0	0	0	$\boldsymbol{\tau}_{x}$	0
$\oplus\oplus\ominus\ominus$	0	$\boldsymbol{\tau}_{yz}$	$\boldsymbol{\tau}_{xyz}$	0	0	$\boldsymbol{\tau}_{yz}$	$\boldsymbol{\tau}_{xyz}$
$\oplus\oplus\oplus\oplus$	0,$\boldsymbol{\tau}_{xyz}$	$\boldsymbol{\tau}_{x}$,$\boldsymbol{\tau}_{yz}$	0,$\boldsymbol{\tau}_{xyz}$	0,$\boldsymbol{\tau}_{xyz}$	0,$\boldsymbol{\tau}_{xyz}$	$\boldsymbol{\tau}_{x}$,$\boldsymbol{\tau}_{yz}$	0,$\boldsymbol{\tau}_{xyz}$
$\oplus\ominus\oplus\ominus$	0,$\boldsymbol{\tau}_{xyz}$	×	×	0,$\boldsymbol{\tau}_{xyz}$	0,$\boldsymbol{\tau}_{xyz}$	×	×

TABLE I: Symmetries of *c*-axis stacked (a) CAF and (b) *d*PSCO. The table gives the lattice translation required for a state to recover itself after a symmetry operation of the magnetic space group $2/m1'$. Symbol × means such a lattice translation does not exist. Translation vector $\boldsymbol{\tau}_x$=(1/2, 0, 0), $\boldsymbol{\tau}_{yz}$=(0, 1/2, 1/2), and $\boldsymbol{\tau}_{xyz}$=(1/2, 1/2, 1/2) in terms of the lattice constant (a, b, c) of the conventional unit cell. Note that the states listed in the last two rows of both (a) and (b) are invariant under a lattice translation of $\boldsymbol{\tau}_{xyz}$, there are thus two possible lattice translations differed by $\boldsymbol{\tau}_{xyz}$.

for a state to recover itself after a symmetry operation of the magnetic point group $2/m1'$: two-fold rotation around z-axis C_{2z}, mirror reflection about ab-plane M_z, inversion I with respect to $(3/4, 1/2, 1/2)$, time-reversal T, $C'_{2z} = TC_{2z}$, $M'_z = TM_z$, and $I' = TI$. The state does not have the corresponding symmetry if it could not recover itself by any lattice translation after a symmetry operation. Note that, because the magnetic moments are aligned in the basal ab plane, without any c-axis component, the time-reversal operator T transforms under the same irreducible representation as C_{2z}, and consequently, the point group symmetry operations C'_{2z}, M'_z, and I' are projected to identity E, I, and M_z, respectively, as shown in Table I(a). The $+--+$ and $++--$ CAF states share the same symmetries and belong to the centrosymmetric orthorhombic magnetic point group $2/m1'$. However, they are inequivalent in the presence of in-plane anisotropy [39, 40], as will be shown in the microscopic model calculations presented in Sec. IIIB. The nonmagnetoelectric $++++$ CAF breaks $\{C_{2z}, M_z, T, I'\}$, while the magnetoelectric $+-+-$ CAF breaks $\{C_{2z}, I, T, M'_z\}$ symmetries. They belong to the magnetic point groups $2'/m'$ and $2'/m$, respectively. It has been argued[41] that both the $++++$ and $+-+-$ CAF can potentially explain the SHG experiment [27] without invoking the loop-currents, and either of them might have been created by the laser pump used in the experiments. The possibility of laser-induced rearrangement of the magnetic stacking, however, has been ruled out by recent comprehensive measurements [35], which show the magnetic stacking pattern is always $+--+$ under the experimental condition before strong external field drives it to be $++++$.

stacking	C_{2z}	M_z	I	T	C'_{2z}	M'_z	I'
$+--+$ / $\oplus\ominus\ominus\oplus$	×	×	✓	×	✓	✓	×
$+--+$ / $\oplus\oplus\ominus\ominus$	×	✓	×	×	✓	×	✓
$+--+$ / $\oplus\oplus\oplus\oplus$	✓	✓	✓	✓	✓	✓	✓
$+--+$ / $\oplus\ominus\oplus\ominus$	✓	×	×	✓	✓	×	×
$++--$ / $\oplus\ominus\ominus\oplus$	×	✓	×	×	✓	×	✓
$++--$ / $\oplus\oplus\ominus\ominus$	×	×	✓	×	✓	✓	×
$++--$ / $\oplus\oplus\oplus\oplus$	✓	✓	✓	✓	✓	✓	✓
$++--$ / $\oplus\ominus\oplus\ominus$	✓	×	×	✓	✓	×	×
$++++$ / $\oplus\ominus\ominus\oplus$	×	×	✓	×	✓	✓	×
$++++$ / $\oplus\oplus\ominus\ominus$	×	×	✓	×	✓	✓	×
$++++$ / $\oplus\oplus\oplus\oplus$	×	×	✓	×	✓	✓	×
$++++$ / $\oplus\ominus\oplus\ominus$	×	×	×	×	✓	×	×
$+-+-$ / $\oplus\ominus\ominus\oplus$	×	✓	×	×	✓	×	✓
$+-+-$ / $\oplus\oplus\ominus\ominus$	×	✓	×	×	✓	×	✓
$+-+-$ / $\oplus\oplus\oplus\oplus$	×	✓	×	×	✓	×	✓
$+-+-$ / $\oplus\ominus\oplus\ominus$	×	×	×	×	✓	×	×

TABLE II: Symmetries of the coexistence states with possible *c*-axis stacking of CAF and *d*PSCO. Symbol ✓/× means the corresponding symmetry is preserved/broken in the coexistence state.

Before performing the symmetry analysis for the *c*-axis stacked hidden *d*PSCO, we define first the notation for its stacking pattern. The staggered IrO_6 octahedra rotation about the c axis results in two kinds of Ir sites, enclosed by the octahedrons rotated clockwise and anticlockwise, respectively, as shown in Fig. 1(a). In a similar vein, the staggered rotation of IrO_6 octahedra gives rise to two kinds of Ir plaquettes, with the enclosed unshaded parallelograms stretched along, respectively, the x and the y axis, as illustrated in Fig 1(b). The circulating pseudospin currents generate staggered pseudospin flux through each Ir plaquette. The direction of the pseudospin flux through these two kinds of Ir plaquettes is denoted by, respectively, red and green symbols at the two different plaquette centers, with $\oplus/\ominus$ corresponding to $\pm c$ axis. The stacking of the *d*PSCO is then characterized by the red symbols in each plane, from top to bottom. For instance, the stacking pattern for the *d*PSCO shown in Fig. 2(a) corresponds to $\oplus\oplus\ominus\ominus$.

The symmetries of the nonmagnetic phases with possible *c*-axis stacked *d*PSCO are summarized in Table I(b). Since the *d*PSCO is invariant under the time-reversal operator T, any operator is identical to its product with T, *e.g.*, $C_{2z} = C'_{2z}$, $M_z = M'_z$, and $I = I'$. As shown in Table I(b), the $\oplus\ominus\ominus\oplus$, $\oplus\oplus\ominus\ominus$, and $\oplus\oplus\oplus\oplus$ *d*PSCO states have all the symmetries of the magnetic point group $2/m1'$, while the $\oplus\ominus\oplus\ominus$ *d*PSCO breaks mirror reflection M_z and inversion I but preserves the symmetries of two-fold rotation C_{2z} and time-reversal T. It is important to note that all of the dPSCO states have the two-fold rotation and time-reversal symmetries. Thus none of them is able to describe the hidden order in *hole-doped* $Sr_2Ir_{1-x}Rh_xO_4$ observed by SHG [27] and polarized neutron scattering [28] measurements. We argue that the physics in the hole-doped Sr_2IrO_4 to be quite different than that on the electron-doped side. The Rh substitution[42–47] of the strongly spin-orbit coupled Ir in the Ir-O plane is very different than the electron doping by La substitution[48–50] in the off-plane charge reservoir layers or surface K doping[16, 17, 19, 51]. Furthermore, a doped hole in Sr_2IrO_4 has a different electronic structure than that of an electron and is more likely to involve higher pseudospin states [52]. We therefore leave the hole-doped Sr_2IrO_4 aside, and consider only the undoped and electron-doped Sr_2IrO_4. Their unconventional low-energy quasiparticle properties observed by ARPES and STM have been described successfully by the hidden order of dPSCO [36] in the two-dimension limit of a single IrO_2 layer. Our focus in this paper is to investigate the effects of dPSCO on the symmetry properties of the three-dimensional systems, which enables a direct comparison to SHG and polarized neutron scattering experiments. At stoichiometry where these experiments have been conducted, the Néel temperature T_N and the hidden order transition temperature T_Ω are very close to each other and barely distinguishable, thus provide us unambiguously only the symmetry information of the ground state, *i.e.*, the coexistence state of CAF and dPSCO.

The coexistence state has a symmetry only if there exist a lattice translation that simultaneously recovers both the CAF and the dPSCO states after the corresponding symmetry operation. Using the symmetries of the CAF and dPSCO summarized in Table I, the symmetries of the coexistence states are readily obtained, with the result given in Table II for all possible c-axis stacking patterns. Remarkably, there is one particular coexistence state, *i.e.*, $+--+/\oplus\oplus\ominus\ominus$ with $+--+$ CAF and $\oplus\oplus\ominus\ominus$ dPSCO, whose magnetism and symmetry are compatible with current experimental observations for undoped Sr_2IrO_4. Its magnetism is $+--+$ stacked CAF, and it breaks the two-fold rotation, inversion, and time-reversal symmetries while preserving the mirror reflection symmetry. These properties make this coexistence state a promising candidate for the ground state of undoped Sr_2IrO_4. Fig. 2(a) shows the structure of the CAF and dPSCO in the $+--+/\oplus\oplus\ominus\ominus$ coexistence state. The structural of dPSCO is illustrated by the symbols of $\oplus$ and $\ominus$ at the center of each Ir plaquette, which denote the direction of the associated pseudospin flux. The motion of the pseudospin-up and pseudospin-down electrons is not drawn here for the simplicity and visibility of the figure. The resultant structures, enclosed in the original unit cell, upon applying two-fold rotation C_{2z}, mirror refection M_z, inversion I, and time-reversal T are shown explicitly in Fig. 2(b-e). It is clear that only the structure in Fig. 2(c) can recover the original structure in Fig. 2(a) after a lattice translation of $\boldsymbol{\tau}_{yz}$=(0,1/2,1/2), while the other three structures could not recover that in Fig. 2(a) by any lattice translation.

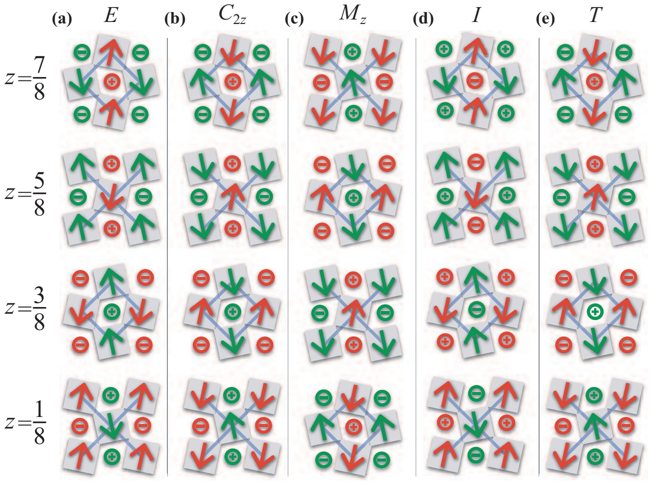

FIG. 2: (a) Structure of Sr_2IrO_4 with $+--+$ canted AFM and $\oplus\oplus\ominus\ominus$ dPSCO. Planes through each IrO_2 layer in the unit cell are shown, with z denoting the position of the layer along the c-axis. Resultant structure, enclosed in the original unit cell, upon applying the following operations contained with in the $2/m1'$ point group: (b) 180° rotation about the c-axis, (c) reflection about a mirror plane normal to the c-axis, (d) time-reversal, and (e) spatial inversion. Only the structure after mirror reflection can recover the original one by a simple lattice translation.

III. MICROSCOPIC MODELS

A. Three-dimensional TB+SOC model

The two-dimensional TB+SOC model constructed in Ref. [36]

$$\mathcal{H}_0 = \sum_{ij,\mu\nu,\sigma} t_{ij}^{\mu\nu,\sigma} d^\dagger_{i\mu\sigma} d_{j\nu\sigma} + \sum_{i\mu\sigma} \epsilon_\mu d^\dagger_{i\mu\sigma} d_{i\mu\sigma} + \lambda_{\rm SOC} \sum_{i,\mu\nu,\sigma\sigma'} \langle\mu|\mathbf{L}|\nu\rangle \cdot \langle\sigma|\mathbf{S}|\sigma'\rangle d^\dagger_{i\mu\sigma} d_{i\nu\sigma'} \qquad (1)$$

provides a faithful description of the DFT band structure [Fig. 3(a)] downfolded to the five low-energy Ir 5d-electron orbitals, as shown in Fig. 3(d). Here, $d^\dagger_{i\mu\sigma}$ creates an electron with spin σ at site i in the μth orbital defined in the local coordinate (X, Y, Z) that rotates with the IrO_6 octahedron, and $\mu = 1(d_{YZ})$, $2(d_{ZX})$, $3(d_{XY})$, $4(d_{3Z^2-R^2})$, and $5(d_{X^2-Y^2})$. The crystalline electric field effects are taken into account in the on-site energy term $\epsilon_{1,\cdots,5} = (0, 0, 202, 3054, 3831)$ meV, with a

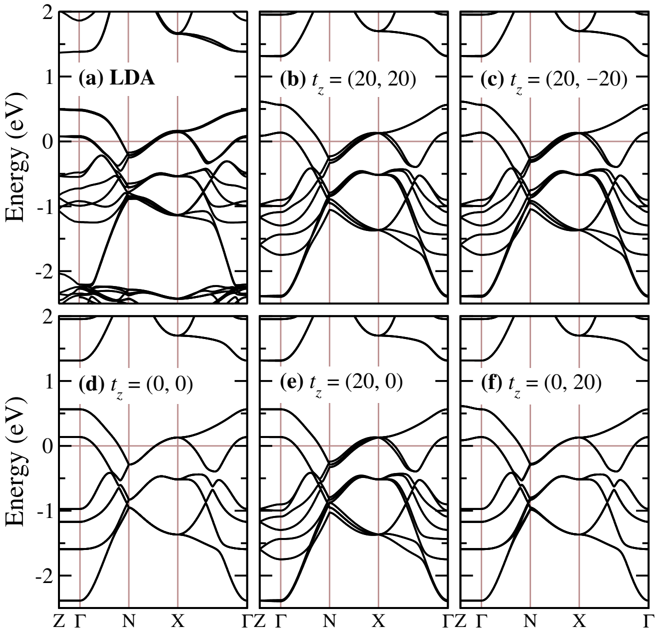

FIG. 3: Comparison of the band structures obtained using (a) LDA and (b-f) the three-dimensional five-orbital TB+SOC model with various inter-layer hoppings $t_z = (t_{z1}, t_{z2})$ given in meV. The high-symmetry points labeled by $\Gamma = (0,0,0)$, X=$(\pi,0,0)$, N=$(\pi/2,\pi/2,0)$, and Z=$(0,0,\pi)$.

separation of $\Delta_c \equiv 10Dq \simeq 3.4$ eV between the t_{2g} and e_g complexes. The strength of atomic SOC $\lambda_{\rm SOC} = 357$ meV. The spin and orbital angular momentum operators, $\mathbf{S}$ and $\mathbf{L}$, have matrix elements, $S^{\eta}_{\sigma\sigma'} = \langle\sigma|\mathbf{S}|\sigma'\rangle$ and $L^{\eta}_{\mu\nu} = \langle\mu|\mathbf{L}|\nu\rangle$, given explicitly in Ref. [36]. The spin-and-orbital-dependent complex hopping integrals $t^{\mu\nu,\sigma}_{ij}$ between sites i and j in the realistic $\mathrm{Sr_2IrO_4}$ with structural distortion are derived from those in the idealized $\mathrm{Sr_2IrO_4}$ without structural distortion $\tilde{t}^{\mu\nu,\sigma}_{ij}$ by transforming the 10×10 hopping matrix, $t_{ij} = \mathcal{R}^{\dagger}_i \tilde{t}_{ij} \mathcal{R}_j$. The operator $\mathcal{R}_i = e^{-iL_z\theta_i} \otimes e^{iS_z\theta_i}$ amounts to a joint spatial rotation from the global (x,y,z) to the local (X,Y,Z) coordinates by θ_i and a spin rotaion by the same angle θ_i. Note that there is a 45° rotation between the x,y axis of the global coordinate defined in this Section and the a,b axis used in Sec. II, as shown in the inset in Fig. 1. In the undistorted idealized systems, the hopping integrals $\tilde{t}^{\mu\nu,\sigma}_{ij}$ are real, spin-independent, and given in Ref. [36] explicitly up to the fifth nearest neighbors in a $\mathrm{IrO_2}$ layer.

To construct a realistic three-dimensional model for $\mathrm{Sr_2IrO_4}$, in addition to the in-plane $\tilde{t}_{ij}$ given in Ref. [36], we include nonzero $\tilde{t}_{ij}$'s on the nearest neighbor (NN) inter-layer bonds, *i.e.*, site i and j from two adjacent $\mathrm{IrO_2}$ layers. Owing to the shift between adjacent $\mathrm{IrO_2}$ ab-planes, as shown in Fig. 2(a), there are eight inter-layer NN sites for each Ir atom, four in the layer right above it and the other four in the layer right below it. The inter-layer hoppings can be limited to the t_{2g} orbitals since the contribution from the e_g orbitals to the low-energy states is negligible small. Furthermore, the inter-layer hoppings involving the planar orbital d_{xy} are expected to be small. In fact, any significant inter-layer intraorbital hopping of the d_{xy} orbital would split the bands around -2 eV below the Fermi level, clearly incompatible with the LDA band structures shown in Fig. 3(a). We thus consider only inter-layer hoppings involving the d_{yz} and d_{zx} orbitals, $t_z = (t_{z1}, t_{z2})$, where t_{z1} and t_{z2} denotes, respectively, the intraorbital and interorbital hoppings. While the intraorbital hoppings are isotropic on the inter-layer NN bonds, the interorbital hoppings are anisotropic, taking values $\pm t_{z2}$ on the four inter-layer NN bonds parallel to the $[1,\pm1,0]$ plane in the (x,y,z) global coordinates.

Figs. 3(b-f) show the electronic structures of the three-dimensional TB+SOC model with various inter-layer hoppings $t_z = (t_{z1}, t_{z2})$, in comparison to the LDA band structure plotted in Fig. 3(a). Note that the band structures for opposite inter-layer hoppings (*i.e.*, $t_z \to -t_z$) are identical, and remain equivalent even in the presence of Hubbard interaction and dPSCO considered in the following subsections. We therefore fix the intraorbital t_{z1} to be positive. Fig. 3(d) displays the band structure of the two-dimensional TB+SOC model without any inter-layer hopping, $t_z = 0$, and Fig. 3(e) and 3(f) show, respectively, the individual effects of the intraorbital t_{z1} and interorbital t_{z2} on the band structure. Clearly, t_{z2} does little to the band structure, while t_{z1} splits the bands and thus captures the essential inter-layer features of the LDA bands displayed in Fig. 3(a). The splitting is about $4t_{z1}$ at N point for the bands right below the Fermi level. Therefore, an intraorbital t_{z1} of 20 meV would reproduce the $\sim$ 78 meV band splitting in the LDA bands. The effects of the interorbital t_{z2} on the band structures are negligible even in the presence of nonzero t_{z1}, as shown in Fig. 3(b) and 3(c). Consequently, t_{z2} remains as a tunable band parameter that shall be determined later by the c-axis stacking of the magnetism.

B. Stacking of canted AFM

To investigate the magnetism in $\mathrm{Sr_2IrO_4}$, we consider the three-dimensional five-orbital Hubbard model $\mathcal{H} = \mathcal{H}_0 + \mathcal{H}_U$, with the electron correlations described by the standard multiorbital Hubbard interactions

$$\begin{aligned}\mathcal{H}_U =& U\sum_{i,\mu}\hat{n}_{i\mu\uparrow}\hat{n}_{i\mu\downarrow} + (U' - J_H/2)\sum_{i,\mu<\nu}\hat{n}_{i\mu}\hat{n}_{i\nu} \qquad (2)\\ &- J_H\sum_{i,\mu\neq\nu}\mathbf{S}_{i\mu}\cdot\mathbf{S}_{i\nu} + J_H\sum_{i,\mu\neq\nu}d^{\dagger}_{i\mu\uparrow}d^{\dagger}_{i\mu\downarrow}d_{i\nu\downarrow}d_{i\nu\uparrow},\end{aligned}$$

where U and U' are the local intraorbital and interorbital Coulomb repulsions and J_H is the Hund's rule coupling

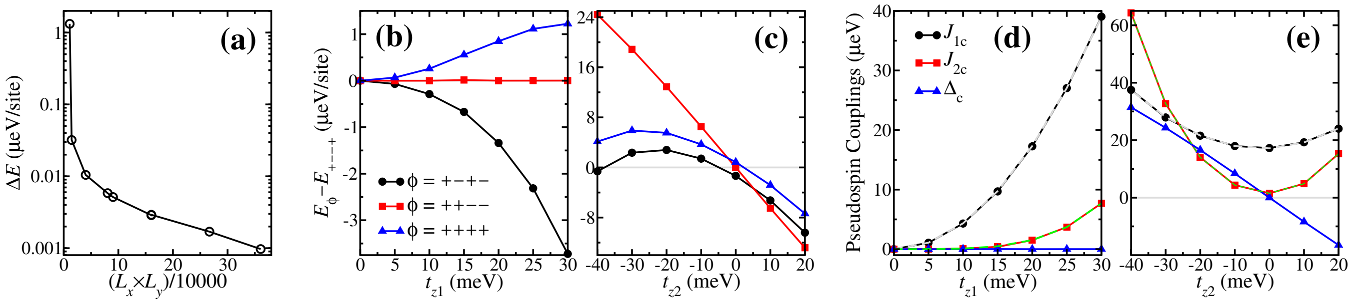

FIG. 4: (a) Energy difference between $(+--+)_a$ and $(++--)_b$ canted AFM as a function of $L_x \times L_y$, the number of in-plane **k**-points. The total number of **k**-points, $L_x \times L_y \times L_z$, in a octant of the three-dimensional reduced Brillouin zone is, for the nine data points from left to right, $121 \times 90 \times 20$, $121 \times 120 \times 110$, $201 \times 200 \times 40$, $284 \times 283 \times 20$, $301 \times 300 \times 60$, $401 \times 400 \times 10$, $401 \times 400 \times 80$, $517 \times 516 \times 6$, and $601 \times 600 \times 10$. The inter-layer hopping $t_z = (20, -20)$ meV. (b) Intraorbital t_{z1} dependence of the canted AFM state energies in the absence of interorbital hopping, $t_{z2} = 0$. (c) Interorbital t_{z2} dependence of the canted AFM state energies with intraorbital $t_{z1} = 20$ meV. Data in (b) and (c) is obtained with $L_x \times L_y \times L_z = 601 \times 600 \times 10$. (d) Intraorbital t_{z1} dependence of the interlayer pseudospin couplings with $t_{z2} = 0$. (e) Interorbital t_{z2} dependence of the interlayer pseudospin couplings with $t_{z1} = 20$ meV. Grey/green dashed lines in (d) and (e) are fits to the data by quadratic/quartic functions.

with the relation of $U = U' + 2J_H$. Note that, in Eq. (2) for the complete set of five d orbitals, J_H should be understood as an average of the exchange interactions of the t_{2g} and e_g orbitals since the difference between them is usually small in cubic systems [53, 54]. The interactions in Eq. (2) are treated within the Hartree-Fock approximations. In the presence of SOC, the Hartree and exchange self-energies induced by $\mathcal{H}_U$ depend on the full spin-orbital-dependent density matrix $n^{\mu\nu}_{i\sigma\sigma'} = \langle d^\dagger_{i\mu\sigma} d_{i\nu\sigma'} \rangle$, which are determined self-consistently in the numerical calculations. Local physical quantities in the ground state can be expressed in terms of $n^{\mu\nu}_{i\sigma\sigma'}$, the local spin density $S^\eta_i = \sum_{\mu,\sigma\sigma'} S^\eta_{\sigma\sigma'} n^{\mu\mu}_{i\sigma\sigma'}$, and the local orbital angular momentum $L^\eta_i = \sum_{\mu\neq\nu,\sigma} n^{\mu\nu}_{i\sigma\sigma} L^\eta_{\mu\nu}$. In all calculations presented in this paper, we choose $(U, J_H) = (1.2, 0.05)$ eV that, in the two-dimensional calculations [36], produces correctly the CAF as the magnetic ground state for the undoped Sr$_2$IrO$_4$, and the low-energy quasiparticle properties in good agreement with ARPES measurements [15].

We first verify numerically the one-to-one correspondence, discussed in the previous section, between the CAF states with FM moment along a axis and those with FM moment along b axis. The direction of the net FM moment can be pinned by choosing appropriate initial values for $n^{\mu\nu}_{i\sigma\sigma'}$. In numerical calculations, an octant of the reduced Brillouin zone, corresponding to the conventional unit cell with eight Ir atoms shown in Fig. 2(a), is discretized evenly into $L_x \times L_y \times L_z$ **k**-points. We obtain these states self-consistently at various $L_x \times L_y \times L_z$ and compare their energies. Fig. 4(a) plots the energy difference between the $(+--+)_a$ and $(++--)_b$ CAF states as a function of the in-plane **k**-point $L_x \times L_y$, with the inter-layer hopping fixed to be $t_z = (20, -20)$ meV. The energy difference is not sensitive to L_z, probably because the inter-layer hoppings t_z are much smaller in amplitude than the in-plane hoppings. Except for the first two data points, the energy difference is less than 0.01 μeV per site, within the resolution of our numerical calculations. We thus conclude that the $(+--+)_a$ and $(++--)_b$ canted AFM states are equivalent, consistent with the symmetry analysis. The correspondences between other states are also verified numerically. To reduce the finite-size effect, we take $L_x \times L_y \times Lz = 601 \times 600 \times 10$ in the rest of the paper.

In the absence of interorbital hopping, $t_{z2} = 0$, the intraorbital t_{z1} dependence of the state energy of $+-+-$, $++--$, and $++++$ CAF is shown in Fig. 4(b), with respect to that of the $+--+$ CAF. Clearly, the $+--+$ and $++--$ CAF are identical in energy at any intraorbital t_{z1}, implying the absence of the in-plane anisotropy. It is thus equivalent for the net FM moment to align in either the a-axis or in the b-axis, in the absence of t_{z2}. The intraorbital t_{z1} energetically favors the $+-+-$ CAF, while disfavors mostly the $++++$ CAF. Fixing intraorbital $t_{z1} = 20$ meV by the ~ 78 meV band splitting in LDA, Fig. 4(c) plots the energies of the CAF states as a function of interorbital t_{z2}. While the $+--+$ CAF is the most unfavored magnetic state on the positive t_{z2} side, there is a wide range on the negative side, $t_{z2} \in (-38, -6)$ meV, where the $+--+$ CAF becomes the lowest in energy, supporting the ground magnetic structure revealed in experiments [2, 26]. Furthermore, the $++++$ CAF is higher in energy by about 5 μeV per site at $t_{z2} = -20$ meV, which agrees remarkably well with the ∼0.3 T external magnetic field required in experiments to align all FM moment along one direction[2].

Within the pseudospin-only models [39, 55], it has been shown that the c-axis stacking of the static long-range magnetic order in the undoped Sr$_2$IrO$_4$ is sta-

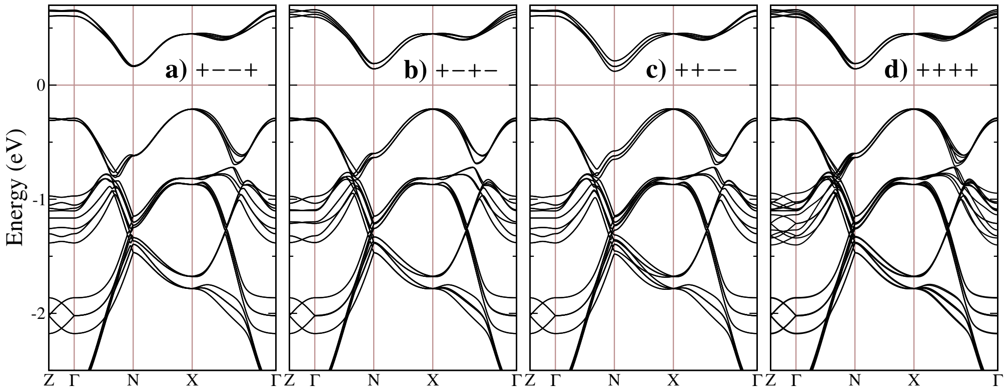

FIG. 5: Comparison between the band dispersions of the CAF states with various c-axis stacking. The inter-layer hoppings $t_z = (20, -20)$ meV and the Hubbard interactions $(U, J) = (1.2, 0.05)$ eV.

bilized by the interplay of interlayer pseudospin couplings, including the first-nearest-interlayer interaction J_{1c}, the second-nearest-interlayer interaction J_{2c}, and the anisotropy Δ_c comes from the anisotropic interlayer interaction[56]. In terms of the effective couplings between the net moments ($\tilde{\mathbf{S}} = \mathbf{L}+2\mathbf{S}$), $j_{1c} = 4J_{1c}\tilde{S}^2 \sin^2\theta$, $j_{2c} = -J_{2c}\tilde{S}^2(\cos^2\theta - \sin^2\theta)$, and $\delta_c = 4\Delta_c\tilde{S}^2\cos^2\theta$, the energies of the $+--+$, $++--$, $+-+-$, and $++++$ CAF states are, respectively, $-\delta_c - j_{2c}$, $\delta_c - j_{2c}$, $-j_{1c}+j_{2c}$, and $j_{1c}+j_{2c}$. In the CAF states obtained self-consistently at Hubbard interactions $(U, J) = (1.2, 0.05)$ eV, the ordered pseudospin moment $\tilde{S} \simeq 0.67\ \mu_B$ and the canting angle $\theta \simeq 22°$. It is readily and instructive to extract, from the Hartree-Fock state energies given in Fig. 4(b) and 4(c), the values of J_{1c}, J_{2c}, and Δ_c. The interlayer pseudospin couplings are plotted in Fig. 4(d) as a function of intraorbital t_{z1} in the absence of interorbital $t_{z2} = 0$, and in Fig. 4(e) as a function of interorbital t_{z2} with the intraorbital hopping fixed to be $t_{z1} = 20$ meV. Clearly, the intraorbital t_{z1} does not generate any anisotropy Δ_c, while the interorbital t_{z2} produces an anisotropy linear in t_{z2}. In the absence of t_{z2}, the intraorbital t_{z1} produces a $J_{1c} \propto t_{z1}^2$ and a $J_{2c} \propto t_{z1}^4$, as shown in Fig. 4(d). At a fixed nonzero intraorbital t_{z1}, the superexchange interactions J_{1c} and J_{2c} generated by interorbital t_{z2} can be well fitted by quadratic and quartic functions of t_{z2} respectively, as shown in Fig. 4(e). These behaviors are consistent with the fact that superexchange interactions J_{1c} and J_{2c} are generate by, respectively, the second-order and quadratic-order perturbations in the inter-layer hoppings. Interestingly, at $t_z = (20, -20)$ meV, the interlayer pseudospin couplings $(J_{1c}, J_{2c}, \Delta_c) = (21.6, 14.0, 16.6)$ μeV are consistent with the values extracted from experiment [39].

Fig. 5 displays the band dispersions of the CAF states with different c-axis stackings. They are all AFM insulators with a similar overall structure. The quasiparticle band below the AFM gap has an eight-fold degeneracy at X point, four of them due to the folding along the c axis of the conventional unit cell and the other two are protected by the two-fold rotation symmetry C_{2a} about the a axis, along which the FM moment aligned. These eight bands behave differently along the X-N direction, which is probably the most pronounced difference among these band structures. They remain degenerate in the $+--+$ CAF, split into three branches in the $++--$ CAF, but split into two branches in the $+-+-$ and $++++$ CAF states.

C. Stacking of *d*PSCO

The physical origin of the dPSCO is still under investigation [36], and out of the scope of the current paper. Therefore, unlike the CAF, its stacking pattern could not be determined self-consistently by including in the Hamiltonian an interaction term from which the dPSCO develops spontaneously. Instead, we determine its c-axis stacking via a variational approach. Explicitly, a variational term for the dPSCO, $\mathcal{H}_\Delta$, is added to the Hamiltonian, $\mathcal{H} = \mathcal{H}_0 + \mathcal{H}_U + \mathcal{H}_\Delta$, with

$$\mathcal{H}_\Delta = i\Delta \sum_{i\in A,\sigma} \sum_{j=i+\delta} \eta_i \tau_{ij} \sigma \left(\gamma^\dagger_{i\sigma}\gamma_{j\sigma} - \chi^\sigma_{ij}\right) + \text{H.c.}, \qquad (3)$$

where the NN vector $\delta = \{\pm\hat{x}, \pm\hat{y}\}$, the standard NN d-wave form factor $\tau_{ij} = (-1)^{i_y + j_y}$, and $\chi^\sigma_{ij} = \langle\gamma^\dagger_{i\sigma}\gamma_{j\sigma}\rangle$ whose presence ensures that the variational term $\mathcal{H}_\Delta$ does not add an elastic part to the state energy. The operator $\gamma_\sigma = \frac{1}{\sqrt{3}}(i\sigma d_{yz,\bar{\sigma}} + d_{zx,\bar{\sigma}} + i d_{xy,\sigma})$ annihilates the $J_{\text{eff}} = 1/2$ doublet in the quasiparticle excitations, $|J = 1/2, J_z = \pm 1/2\rangle = \gamma^\dagger_\pm|0\rangle$. The c-axis stacking of dPSCO is then controlled by η_i as it takes on values of ± 1 for Ir site i in different IrO$_2$ layers. For example, to generate the $\oplus\oplus\ominus\ominus$ stacking pattern for dPSCO, η_i take the value of $+1$, $+1$, -1, and -1, respectively, for

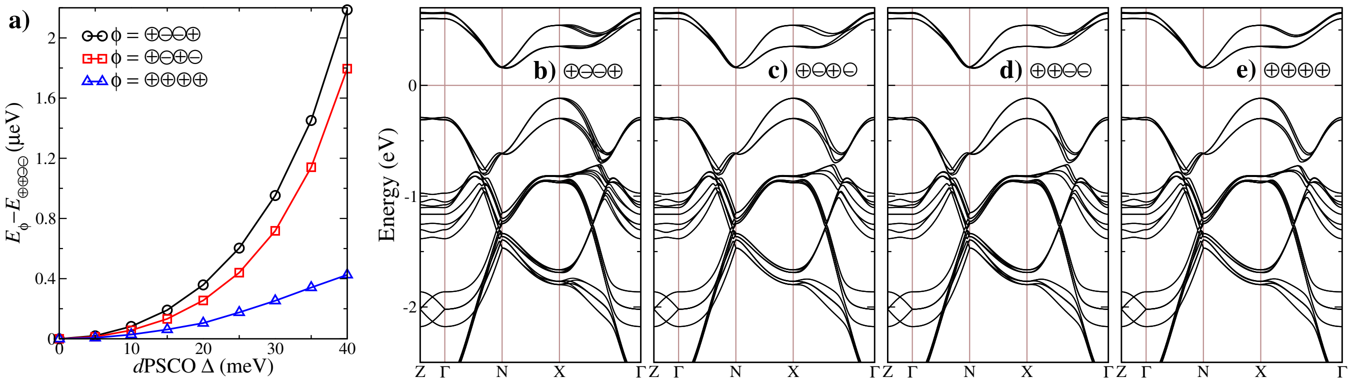

FIG. 6: (a) The state energies of the coexistence states as a function of the dPSCO order Δ. The stacking pattern of the canted AFM is fixed to be $+--+$, and the interlayer hopping $t_z = (20, -20)$ meV. (b-e) Comparison of the band dispersions of the coexistence states with various c-axis stacking of dPSCO ($\Delta = 30$ meV).

lattice site i in the four IrO_2 layers. We fix the the stacking pattern of CAF to be $+--+$, and try to find the energetically preferred stacking pattern of dPSCO in the coexistence state.

The interlayer hoppings are chosen to be $t_z = (20, -20)$ meV where the $+--+$ CAF is the magnetic ground stare. At a given strength of dPSCO, Δ, we obtain the coexistence states of $+--+$ CAF with four possible c-axis stacked dPSCO self-consistently, and then compare their energies to find the preferred stacking pattern for the dPSCO. The energies of the coexistence states with $\oplus\ominus\ominus\oplus$, $\oplus\ominus\oplus\ominus$, and $\oplus\oplus\oplus\oplus$ dPSCO are plotted in Fig. 6(a) as a function of Δ, with respect to that of the coexistence state with $\oplus\oplus\ominus\ominus$ dPSCO. It is clear that the $+--+ / \oplus\oplus\ominus\ominus$ coexistence state is energetically favored over all other coexistence states and, as shown in Sec. II, its symmetry is compatible with available experimental observations on undoped Sr_2IrO_4 below the Néel temperature T_N.

The band dispersions of the four coexistence states with $+--+$ CAF are plotted in Figs. 6(b-e) for $\Delta = 30$ meV. The dPSCO order breaks the C_{2a} symmetry, splits the eight-fold degenerate band at X point into two four-fold degenerate branches, giving rise to a band splitting $\sim$ 200 meV at X point. We note that the C_{2a} symmetry is broken by the staggered tetragonal distortion of the IrO_6 octahedra at temperatures above T_Ω in undoped Sr_2IrO_4 [23–26]. However, the tetragonal distortion would split the degenerate bands evenly by a constant along N-X, thus unable to capture the unconventional quasiparticle properties of Sr_2IrO_4 in both the undoped magnetic insulating phase and the electron-doped nonmagnetic phase.

IV. DISCUSSIONS AND SUMMARIES

The existence and the nature of a hidden order in Sr_2IrO_4 have been under intensive debate. After the observation of the anomalous SHG signal [27], polarized neutron diffraction [28] and muon spin relaxation [29] measurements performed on undoped and hole-doped Sr_2IrO_4 revealed broken time-reversal symmetry below T_Ω. Furthermore, magnetic resonant X-ray scattering measurement [50] conducted on the electron-doped Sr_2IrO_4 has uncovered a unidirectional spin density wave state in the pseudogap phase. These experimental observations support the idea that the pseudogap is associated with a symmetry-breaking hidden order. On the other hand, alternative explanations without invoking loop currents were proposed for the anomalous SHG signal, including laser-induced rearrangement of the magnetic stacking and enhanced sensitivity to surface rather than bulk magnetism [41]. More recent comprehensive experiments [35] conducted on undoped Sr_2IrO_4 have ruled out the possibility of laser-induced rearrangement of the magnetic stacking, and suggest that the surface-magnetization induced electric-dipole process in the SHG experiments can be strongly enhanced by SOC. However, the existence of a hidden order in Sr_2IrO_4 remains as a possible explanation for the experimental observations of symmetry breaking and unconventional quasiparticle excitations.

In this work, we have shown that the coexistence state of $+--+$ CAF and $\oplus\oplus\ominus\ominus$ dPSCO has all the symmetry properties compatible with the available experimental observations on the undoped Sr_2IrO_4 below the Néel temperature T_N. It is a magnetoelectric state that breaks the two-fold rotation C_{2z}, inversion I, and time-reversal T symmetries. We then demonstrated its microscopic realization in a realistic three-dimensional Hubbard model with spin-orbit coupling and structural distortion. Together with the fact that the highly unconventional quasiparticle properties observed in both the parent and electron-doped $\mathrm{Sr_2IrO_4}$ can be described remarkably well by the dPSCO [36], the latter offers a promising candidate for the hidden order responsible for the pseudogap phase in the undoped and electron-doped iridates. Since the Néel temperature T_N and the hidden order transition temperature T_Ω are very close to each other in undoped $\mathrm{Sr_2IrO_4}$, available experiments could not tell us unambiguously the symmetry properties of the pseudogap phase. It is thus very desirable to carry out the optical SHG and neutron scattering experiments on the pseudogap phase in electron-doped $\mathrm{Sr_2IrO_4}$. In the absence of magnetism, the dPSCO would preserve the spatial inversion and time-reversal symmetries, but lower the four-fold rotation symmetry to two-fold C_{2z} due to the d-wave form factor. It would be interesting to calculate the magnetic excitations in the nonmagnetic dPSCO state and make comparison to magnetic resonant X-ray scattering observations [50].

ACKNOWLEDGMENTS

YH, JD, and SZ are supported by the Strategic Priority Research Program of CAS (Grant No. XDB28000000) and the National Natural Science Foundation of China (Grants No. 11974362 and No. 12047503). ZW is supported by the U.S. Department of Energy, Basic Energy Sciences (Grant No. DE-FG02-99ER45747). Numerical calculations in this work were performed on the HPC Cluster of ITP-CAS.

---

[*] These two authors contribute equally.

[†] Corresponding author: wangzi@bc.edu

[‡] Corresponding author: zhousen@itp.ac.cn

[1] B. J. Kim, H. Jin, S. J. Moon, J.-Y. Kim, B.-G. Park, C. S. Leem, J. Yu, T. W. Noh, C. Kim, S.-J. Oh, et al., Novel $J_{\mathrm{eff}} = 1/2$ Mott State Induced by Relativistic Spin-Orbit Coupling in $\mathrm{Sr_2IrO_4}$, Phys. Rev. Lett. **101**, 076402 (2008).

[2] B. J. Kim, H. Ohsumi, T. Komesu, S. Sakai, T. Morita, H. Takagi, and T. Arima, Phase-Sensitive Observation of a Spin-Orbital Mott State in Sr2IrO4, Science **323**, 1329 (2009), ISSN 0036-8075.

[3] D. Pesin and L. Balents, Mott physics and band topology in materials with strong spin–orbit interaction, Nature Physics **6**, 376 (2010).

[4] W. Witczak-Krempa, G. Chen, Y. B. Kim, and L. Balents, Correlated quantum phenomena in the strong spin-orbit regime, Annu. Rev. Condens. Matter Phys. **5**, 57 (2014).

[5] J. G. Rau, E. K.-H. Lee, and H.-Y. Kee, Spin-Orbit Physics Giving Rise to Novel Phases in Correlated Systems: Iridates and Related Materials, Annual Review of Condensed Matter Physics **7**, 195 (2016).

[6] R. Schaffer, E. K.-H. Lee, B.-J. Yang, and Y. B. Kim, Recent progress on correlated electron systems with strong spin–orbit coupling, Reports on Progress in Physics **79**, 094504 (2016).

[7] S. M. Winter, A. A. Tsirlin, M. Daghofer, J. van den Brink, Y. Singh, P. Gegenwart, and R. Valenti, Models and materials for generalized Kitaev magnetism, Journal of Physics: Condensed Matter **29**, 493002 (2017).

[8] M. Hermanns, I. Kimchi, and J. Knolle, Physics of the Kitaev model: Fractionalization, dynamic correlations, and material connections, Annual Review of Condensed Matter Physics **9**, 17 (2018).

[9] J. Dai, E. Calleja, G. Cao, and K. McElroy, Local density of states study of a spin-orbit-coupling induced Mott insulator $\mathrm{Sr_2IrO_4}$, Phys. Rev. B **90**, 041102 (2014).

[10] J. Kim, D. Casa, M. H. Upton, T. Gog, Y.-J. Kim, J. F. Mitchell, M. van Veenendaal, M. Daghofer, J. van den Brink, G. Khaliullin, et al., Magnetic Excitation Spectra of $\mathrm{Sr_2IrO_4}$ Probed by Resonant Inelastic X-Ray Scattering: Establishing Links to Cuprate Superconductors, Phys. Rev. Lett. **108**, 177003 (2012).

[11] F. Wang and T. Senthil, Twisted Hubbard Model for $\mathrm{Sr_2IrO_4}$: Magnetism and Possible High Temperature Superconductivity, Phys. Rev. Lett. **106**, 136402 (2011).

[12] Y. Yang, W.-S. Wang, J.-G. Liu, H. Chen, J.-H. Dai, and Q.-H. Wang, Superconductivity in doped $\mathrm{Sr_2IrO_4}$: A functional renormalization group study, Phys. Rev. B **89**, 094518 (2014).

[13] H. Watanabe, T. Shirakawa, and S. Yunoki, Monte Carlo Study of an Unconventional Superconducting Phase in Iridium Oxide J_{eff}=1/2 Mott Insulators Induced by Carrier Doping, Phys. Rev. Lett. **110**, 027002 (2013).

[14] Z. Y. Meng, Y. B. Kim, and H.-Y. Kee, Odd-Parity Triplet Superconducting Phase in Multiorbital Materials with a Strong Spin-Orbit Coupling: Application to Doped $\mathrm{Sr_2IrO_4}$, Phys. Rev. Lett. **113**, 177003 (2014).

[15] A. de la Torre, S. McKeown Walker, F. Y. Bruno, S. Riccó, Z. Wang, I. Gutierrez Lezama, G. Scheerer, G. Giriat, D. Jaccard, C. Berthod, et al., Collapse of the Mott Gap and Emergence of a Nodal Liquid in Lightly Doped $\mathrm{Sr_2IrO_4}$, Phys. Rev. Lett. **115**, 176402 (2015).

[16] Y. K. Kim, O. Krupin, J. D. Denlinger, A. Bostwick, E. Rotenberg, Q. Zhao, J. F. Mitchell, J. W. Allen, and B. J. Kim, Fermi arcs in a doped pseudospin-1/2 Heisenberg antiferromagnet, Science **345**, 187 (2014), ISSN 0036-8075.

[17] Y. J. Yan, M. Q. Ren, H. C. Xu, B. P. Xie, R. Tao, H. Y. Choi, N. Lee, Y. J. Choi, T. Zhang, and D. L. Feng, Electron-Doped $\mathrm{Sr_2IrO_4}$: An Analogue of Hole-Doped Cuprate Superconductors Demonstrated by Scanning Tunneling Microscopy, Phys. Rev. X **5**, 041018 (2015).

[18] I. Battisti, K. M. Bastiaans, V. Fedoseev, A. De La Torre, N. Iliopoulos, A. Tamai, E. C. Hunter, R. S. Perry, J. Zaanen, F. Baumberger, et al., Universality of pseudogap and emergent order in lightly doped Mott insulators, Nature Physics **13**, 21 (2017).

[19] Y. K. Kim, N. Sung, J. Denlinger, and B. Kim, Observation of ad-wave gap in electron-doped $\mathrm{Sr_2\ IrO_4}$, Nature Physics **12**, 37 (2016).

[20] H. Zhao, S. Manna, Z. Porter, X. Chen, A. Uzdejczyk, J. Moodera, Z. Wang, S. D. Wilson, and I. Zeljkovic, Atomic-scale fragmentation and collapse of antiferromagnetic order in a doped Mott insulator, Nature Physics **15**,

1267 (2019).

[21] S. Boseggia, H. C. Walker, J. Vale, R. Springell, Z. Feng, R. S. Perry, M. M. Sala, H. M. Rønnow, S. P. Collins, and D. F. McMorrow, Locking of iridium magnetic moments to the correlated rotation of oxygen octahedra in Sr2IrO4revealed by x-ray resonant scattering, Journal of Physics: Condensed Matter **25**, 422202 (2013).

[22] M. K. Crawford, M. A. Subramanian, R. L. Harlow, J. A. Fernandez-Baca, Z. R. Wang, and D. C. Johnston, Structural and magnetic studies of Sr_2IrO_4, Phys. Rev. B **49**, 9198 (1994).

[23] F. Ye, S. Chi, B. C. Chakoumakos, J. A. Fernandez-Baca, T. Qi, and G. Cao, Magnetic and crystal structures of Sr_2IrO_4: A neutron diffraction study, Phys. Rev. B **87**, 140406 (2013).

[24] C. Dhital, T. Hogan, Z. Yamani, C. de la Cruz, X. Chen, S. Khadka, Z. Ren, and S. D. Wilson, Neutron scattering study of correlated phase behavior in Sr_2IrO_4, Phys. Rev. B **87**, 144405 (2013).

[25] D. H. Torchinsky, H. Chu, L. Zhao, N. B. Perkins, Y. Sizyuk, T. Qi, G. Cao, and D. Hsieh, Structural Distortion-Induced Magnetoelastic Locking in Sr_2IrO_4 Revealed through Nonlinear Optical Harmonic Generation, Phys. Rev. Lett. **114**, 096404 (2015).

[26] S. Boseggia, R. Springell, H. C. Walker, H. M. Rønnow, C. Rüegg, H. Okabe, M. Isobe, R. S. Perry, S. P. Collins, and D. F. McMorrow, Robustness of Basal-Plane Antiferromagnetic Order and the $J_{\rm eff}$=1/2 State in Single-Layer Iridate Spin-Orbit Mott Insulators, Phys. Rev. Lett. **110**, 117207 (2013).

[27] L. Zhao, D. Torchinsky, H. Chu, V. Ivanov, R. Lifshitz, R. Flint, T. Qi, G. Cao, and D. Hsieh, Evidence of an odd-parity hidden order in a spin–orbit coupled correlated iridate, Nature Physics **12**, 32 (2016).

[28] J. Jeong, Y. Sidis, A. Louat, V. Brouet, and P. Bourges, Time-reversal symmetry breaking hidden order in Sr_2 (Ir, Rh) O_4, Nature communications **8**, 1 (2017).

[29] C. Tan, Z. F. Ding, J. Zhang, Z. H. Zhu, O. O. Bernal, P. C. Ho, A. D. Hillier, A. Koda, H. Luetkens, G. D. Morris, et al., Slow magnetic fluctuations and critical slowing down in $Sr_2Ir_{1-x}Rh_xO_4$, Phys. Rev. B **101**, 195108 (2020).

[30] H. Murayama, K. Ishida, R. Kurihara, T. Ono, Y. Sato, Y. Kasahara, H. Watanabe, Y. Yanase, G. Cao, Y. Mizukami, et al., Bond Directional Anapole Order in a Spin-Orbit Coupled Mott Insulator $Sr_2(Ir_{1-x}Rh_x)O_4$, Phys. Rev. X **11**, 011021 (2021).

[31] C. M. Varma, Non-Fermi-liquid states and pairing instability of a general model of copper oxide metals, Phys. Rev. B **55**, 14554 (1997).

[32] C. M. Varma, Theory of the pseudogap state of the cuprates, Phys. Rev. B **73**, 155113 (2006).

[33] C. M. Varma, Pseudogap in cuprates in the loop-current ordered state, Journal of Physics: Condensed Matter **26**, 505701 (2014).

[34] S. J. Moon, M. W. Kim, K. W. Kim, Y. S. Lee, J.-Y. Kim, J.-H. Park, B. J. Kim, S.-J. Oh, S. Nakatsuji, Y. Maeno, et al., Electronic structures of layered perovskite Sr_2MO_4 (M = Ru, Rh, and Ir), Phys. Rev. B **74**, 113104 (2006).

[35] K. L. Seyler, A. de la Torre, Z. Porter, E. Zoghlin, R. Polski, M. Nguyen, S. Nadj-Perge, S. D. Wilson, and D. Hsieh, Spin-orbit-enhanced magnetic surface second-harmonic generation in Sr_2IrO_4, Phys. Rev. B **102**, 201113 (2020).

[36] S. Zhou, K. Jiang, H. Chen, and Z. Wang, Correlation Effects and Hidden Spin-Orbit Entangled Electronic Order in Parent and Electron-Doped Iridates Sr_2IrO_4, Phys. Rev. X **7**, 041018 (2017).

[37] J. W. Han, S.-W. Kim, W. S. Kyung, C. Kim, G. Cao, X. Chen, S. D. Wilson, S. Cheon, and J. S. Lee, Nonsymmorphic Dirac semimetal and carrier dynamics in the doped spin-orbit-coupled Mott insulator Sr_2IrO_4, Phys. Rev. B **102**, 041108 (2020).

[38] S.-W. Kim, M. Kang, and S. Cheon, Low-energy electrodynamics of Dirac semimetal phases in the doped Mott insulator Sr_2IrO_4, Phys. Rev. B **103**, 045116 (2021).

[39] J. Porras, J. Bertinshaw, H. Liu, G. Khaliullin, N. H. Sung, J.-W. Kim, S. Francoual, P. Steffens, G. Deng, M. M. Sala, et al., Pseudospin-lattice coupling in the spin-orbit Mott insulator Sr_2IrO_4, Phys. Rev. B **99**, 085125 (2019).

[40] H. Liu and G. Khaliullin, Pseudo-Jahn-Teller Effect and Magnetoelastic Coupling in Spin-Orbit Mott Insulators, Phys. Rev. Lett. **122**, 057203 (2019).

[41] S. Di Matteo and M. R. Norman, Magnetic ground state of Sr_2IrO_4 and implications for second-harmonic generation, Phys. Rev. B **94**, 075148 (2016).

[42] T. F. Qi, O. B. Korneta, L. Li, K. Butrouna, V. S. Cao, X. Wan, P. Schlottmann, R. K. Kaul, and G. Cao, Spin-orbit tuned metal-insulator transitions in single-crystal $Sr_2Ir_{1-x}Rh_xO_4$ ($0 \leq x \leq 1$), Phys. Rev. B **86**, 125105 (2012).

[43] J. P. Clancy, A. Lupascu, H. Gretarsson, Z. Islam, Y. F. Hu, D. Casa, C. S. Nelson, S. C. LaMarra, G. Cao, and Y.-J. Kim, Dilute magnetism and spin-orbital percolation effects in $Sr_2Ir_{1-x}Rh_xO_4$, Phys. Rev. B **89**, 054409 (2014).

[44] F. Ye, X. Wang, C. Hoffmann, J. Wang, S. Chi, M. Matsuda, B. C. Chakoumakos, J. A. Fernandez-Baca, and G. Cao, Structure symmetry determination and magnetic evolution in $Sr_2Ir_{1-x}Rh_xO_4$, Phys. Rev. B **92**, 201112 (2015).

[45] Y. Cao, Q. Wang, J. A. Waugh, T. J. Reber, H. Li, X. Zhou, S. Parham, S.-R. Park, N. C. Plumb, E. Rotenberg, et al., Hallmarks of the Mott-metal crossover in the hole-doped pseudospin-1/2 Mott insulator Sr2IrO4., Nature Communications **7**, 11367 (2016).

[46] V. Brouet, J. Mansart, L. Perfetti, C. Piovera, I. Vobornik, P. Le Fèvre, F. m. c. Bertran, S. C. Riggs, M. C. Shapiro, P. Giraldo-Gallo, et al., Transfer of spectral weight across the gap of Sr_2IrO_4 induced by La doping, Phys. Rev. B **92**, 081117 (2015).

[47] S. Chikara, G. Fabbris, J. Terzic, G. Cao, D. Khomskii, and D. Haskel, Charge partitioning and anomalous hole doping in Rh-doped Sr_2IrO_4, Phys. Rev. B **95**, 060407 (2017).

[48] H. Gretarsson, N. H. Sung, J. Porras, J. Bertinshaw, C. Dietl, J. A. N. Bruin, A. F. Bangura, Y. K. Kim, R. Dinnebier, J. Kim, et al., Persistent Paramagnons Deep in the Metallic Phase of $Sr_{2-x}La_xIrO_4$, Phys. Rev. Lett. **117**, 107001 (2016).

[49] X. Chen, T. Hogan, D. Walkup, W. Zhou, M. Pokharel, M. Yao, W. Tian, T. Z. Ward, Y. Zhao, D. Parshall, et al., Influence of electron doping on the ground state of $(Sr_{1-x}La_x)_2IrO_4$, Phys. Rev. B **92**, 075125 (2015).

[50] X. Chen, J. L. Schmehr, Z. Islam, Z. Porter, E. Zoghlin, K. Finkelstein, J. P. Ruff, and S. D. Wilson, Unidirectional spin density wave state in metallic

$(Sr_{1-x}La_x)_2IrO_4$, Nature communications **9**, 1 (2018).

[51] M. Ge, T. F. Qi, O. B. Korneta, D. E. De Long, P. Schlottmann, W. P. Crummett, and G. Cao, Lattice-driven magnetoresistivity and metal-insulator transition in single-layered iridates, Phys. Rev. B **84**, 100402 (2011).

[52] J. Bertinshaw, Y. Kim, G. Khaliullin, and B. Kim, Square Lattice Iridates, Annual Review of Condensed Matter Physics **10**, 315 (2019).

[53] E. Pavarini, Electronic Structure Calculations with LDA +DMFT. In: Bach V., Delle Site L. (eds) Many-Electron Approaches in Physics, Chemistry and Mathematics: A Multidisciplinary View. Springer, Cham. (2014).

[54] M. E. A. Coury, S. L. Duarev, W. M. C. Foulkes, A. P. Horsfield, P.-W. Ma, and J. S. Spencer, Hubbard-like Hamiltonians for interacting electrons in *s*, *p*, and *d* orbitals, Phys. Rev. B **93**, 075101 (2016).

[55] T. Takayama, A. Matsumoto, G. Jackeli, and H. Takagi, Model analysis of magnetic susceptibility of Sr_2IrO_4: A two-dimensional $J_{\text{eff}} = \frac{1}{2}$ Heisenberg system with competing interlayer couplings, Phys. Rev. B **94**, 224420 (2016).

[56] V. M. Katukuri, V. Yushankhai, L. Siurakshina, J. van den Brink, L. Hozoi, and I. Rousochatzakis, Mechanism of Basal-Plane Antiferromagnetism in the Spin-Orbit Driven Iridate Ba_2IrO_4, Phys. Rev. X **4**, 021051 (2014).